https://dx.doi.org/10.1016/j.enggeo.2020.105870

Simulating retrogressive slope failure using two different smoothed particle finite element methods: a comparative study

Yin-Fu JIN[1,2], **Zhen-Yu YIN**[1*] and **Wei-Hai YUAN**[3]

Affiliation:

[1] Department of Civil and Environmental Engineering, The Hong Kong Polytechnic University, Hung Hom, Kowloon, Hong Kong, China

[2] Southern Marine Science and Engineering Guangdong Laboratory (Guangzhou), No.1119, Haibin Rd., Nansha District, Guangzhou, China

[3] College of Mechanics and Materials, Hohai University, Nanjing, China

[*] Corresponding author: Dr Zhen-Yu Yin, Tel. +852 34008470, Fax +852 23346389, E-mail: zhenyu.yin@polyu.edu.hk; zhenyu.yin@gmail.com

Abstract: Various smoothed particle finite element methods (SPFEMs) have been developed to simulate large deformation problems, but their efficiency and accuracy in simulating progressive landslides in sensitive clays have remained unclear. In this study, a series of numerical analyses are carried out to investigate the development of retrogressive failures by two SPFEMs (an edge-based strain smoothing PFEM, ESPFEM, and a node-based strain smoothing PFEM, NSPFEM) in view of their outstanding performance in large deformation analysis. A strain-softening Mohr–Coulomb (MC) model is adopted to simulate the behaviour of sensitive clays during landslide, assuming a Poisson's ratio of 0.49 to ensure undrained conditions. The influence of mesh density on the development of retrogressive failure is evaluated for two SPFEMs. Numerical analyses of three mesh sizes (0.2 m, 0.15 m and 0.12 m) are carried out sequentially, with all results demonstrating that (1) the spread retrogressive landslides with horsts and grabens can be achieved by both SPFEMs with the adopted soil model, (2) run-out and retrogression distances decrease as mesh density increases for both methods, (3) retrogressive collapse occurs earlier for ESPFEM but is delayed for NSPFEM with increased mesh density, (4) NSPFEM allows faster calculations and reduces mesh dependency problems when compared with ESPFEM and (5) the increase of shape factor can accelerate retrogressive failure in landslides. Finally, a real landslide in sensitive clay at Sainte-Monique, Quebec, is simulated to demonstrate ESPFEM's computational efficiency and accuracy.

Key words: strain smoothing; particle finite element method; large deformation; retrogressive failure; landslide; sensitive clay

1 Introduction

Progressive landslides in sensitive clays are commonplace, being seen from eastern Canada to Scandinavia (Crawford 1968; Geertsema et al. 2006; Locat et al. 2011; Quinn et al. 2012; Wang 2019). According to (Tavenas 1984) and (Karlsrud et al. 1985), such landslides can be divided into four main types: single rotational slides, multiple retrogressive slides, translational progressive landslides and spreads (Cruden and Varnes 1996). In these landslides, ground movement occurs rapidly, with failure propagating in an undrained condition. Moreover, the sensitive clay where they occur exhibits strong strain-softening behaviour resulting from undrained shear (Dey et al. 2015a; Locat et al. 2013; Quinn et al. 2012; Tran and Sołowski 2019; Troncone 2005; Wang 2019; Wang et al. 2016, 2018). These landslides are generally triggered by natural phenomena, such as gradual erosion near the toe of the slope (Yang et al. 2019a, b, c; Yang et al. 2019d).

Many such large-scale landslides involve large deformation. Aided by on-going increases in computing power, numerical simulations have become the standard method for analysing geomechanics and related fields. Among these, the finite element method (FEM) features prominently in engineering practice (Jin et al. 2017; Jin et al. 2018a; Jin et al. 2018b; Jin et al. 2019; Mohammadi and Taiebat 2016; Shen et al. 2017; Shen and Xu 2011; Troncone et al. 2014; Wu et al. 2017; Yin et al. 2018; Zhuang et al. 2020). For FEM, however, excessive deformation of a mesh can produce numerical inaccuracies, to the point of making calculation impossible for large deformation problems. Many researchers have used continuous remeshing and mapping of stresses from old methods to new to deal with very large deformation (using commercial finite element programs with purpose-built submodules), but such methods are time-consuming and tedious. The particle finite element method (PFEM), however, is useful in solving large deformation problems (Yuan et al. 2019; Zhang et al. 2018a; Zhang et al. 2018b; Zhang et al. 2018c). Smoothed PFEM (SPFEM), which offers advantages over PFEM because of its use of a lower-order element while retaining calculation accuracy, is thus suitable for simulation of landslides.

In this study, the retrogressive failure of a slope is simulated using two different SPFEMs: an edge-based strain smoothing PFEM and a node-based strain smoothing PFEM. After briefly introducing these SPFEMs, a typical retrogressive landslide is simulated using a strain–softening

model, using three mesh densities. Shape factor's effect on soil destructuration rate is also investigated, and the SPFEMs' performance is evaluated and compared among all simulations. Finally, a real landslide in sensitive clay at Sainte-Monique, Quebec, is simulated.

2 Smoothed particle finite element method SPFEM

2.1 Brief introduction of explicit PFEM

The key feature of PFEM is that the continuum medium is represented as a cloud of "particles". The particles carry and transport all the information of the continuum medium, which can freely move and even separate from the continuum to which they originally belong. In fact, the PFEM is actually an updated Lagrangian approach with frequent remeshing by the Delaunay triangulation method to overcome the problems of mesh distortion. Therefore, the PFEM inherits both the mesh-free particle methods and the traditional FEMs, which is suitable for solving large deformation problems.

In PFEM, the problem domain is first discretized into a cloud of particles. Then, on the basis of particles, the triangular elements are generated through Delaunay triangulation and the alpha-shape technique is employed to remove elements that do not meet the requirements. Next, the governing equations are solved using a standard finite element method, such as the Newton–Raphson procedure (Carbonell et al. 2009). Apart from the Newton–Raphson procedure, the explicit time integration procedure (Yuan et al. 2019) and mathematical programming (Zhang et al. 2018b; Zhang et al. 2017; Zhang et al. 2018c) can also be adopted to solve the governing equations. Finally, information related to particles is updated and the convergence criterion is checked. The details of the original PFEM can be found in (Carbonell et al. 2009; Zhang et al. 2014; Zhang et al. 2015). The standard algorithm of the PFEM contains the following steps;

[1] Start the calculation;
[2] Discretise the problem domain by a cloud of particles;
[3] Generate the mesh by Delaunay triangulation method;
[4] Identify the problem domain using the alpha-shape technique;
[5] Transfer the information from the mesh of last time step to the new mesh of current time step;

[6] Solve the governing equations;
[7] Update the stresses and variables of integration points, the velocities and accelerations of nodes;
[8] Update the position of particles to construct a new cloud of particles;
[9] Check the stop criterion. If yes, stop the calculation; if not, go back to step 3.

2.2 Edge-based strain smoothing PFEM - ESPFEM

To overcome the volumetric locking problem caused by the strain constant in 3-node triangular elements, a simple and effective strain-smoothed element method, developed by (Lee and Lee 2018) was employed in the original PFEM (see Fig. 1). Based on that, the edge-based SPFEM (ESPFEM) was developed by (Jin et al. 2020). The strains of neighbouring elements (up to three) are used through the element edges to smooth the target element (see Fig. 1a) where $\boldsymbol{\varepsilon}^{(e)}$ is the strain of concerned element and $\boldsymbol{\varepsilon}^{(k)}$ is the strain of the *k*th neighbouring element. Thus, the smoothed strains are defined as:

$$\hat{\boldsymbol{\varepsilon}}^{(k)} = \frac{1}{A^{(e)} + A^{(k)}}\left(A^{(e)}\boldsymbol{\varepsilon}^{(e)} + A^{(k)}\boldsymbol{\varepsilon}^{(k)}\right), \text{ with } k = 1, 2, 3 \tag{1}$$

where $A^{(e)}$ and $A^{(k)}$ are the areas of the target element and the *k*th neighbouring element, respectively, see Fig. 1(b). Note that if no neighbouring element corresponding to the *k*th edge of the target element is found, $\hat{\boldsymbol{\varepsilon}}^{(k)}=\boldsymbol{\varepsilon}^{(e)}$ is adopted.

The obtained smoothed strain values in Eq.(1) are directly assigned to the Gauss integration points (*a*, *b*, and *c* in Fig. 1c) of the target element using the following equations, as shown in Fig. 1(d).

$$\begin{aligned} \boldsymbol{\varepsilon}^{a} &= \frac{1}{2}\left(\hat{\boldsymbol{\varepsilon}}^{(1)} + \hat{\boldsymbol{\varepsilon}}^{(3)}\right) \\ \boldsymbol{\varepsilon}^{b} &= \frac{1}{2}\left(\hat{\boldsymbol{\varepsilon}}^{(1)} + \hat{\boldsymbol{\varepsilon}}^{(2)}\right) \\ \boldsymbol{\varepsilon}^{c} &= \frac{1}{2}\left(\hat{\boldsymbol{\varepsilon}}^{(2)} + \hat{\boldsymbol{\varepsilon}}^{(3)}\right) \end{aligned} \tag{2}$$

In ESPFEM, the edge-based strain smoothing method has a close-to-exact stiffness, which often offers super-convergent and very accurate solutions (Zeng and Liu 2018).

2.3 Node-based strain smoothing PFEM - NSPFEM

A node-based explicit SPFEM (NSPFEM) presented by (Yuan et al. 2019) was adopted herein. More details about NSPFEM can be found in (Yuan et al. 2019; Zhang et al. 2018a). In this study, the NSPFEM was re-programmed in Julia language by authors for a fair comparison to ESPFEM. Compared to the original PFEM, some important features of NSPFEM include: (1) the use of node-based strain smoothing technique proposed by (Liu et al. 2007) to avoid the volumetric locking effects of low order elements (see Fig. 1(e)); (2) the use of a nodal integration technique to avoid the frequent variables transformation between old mesh and new mesh. However, compared to ESPFEM, the node-based strain smoothing method adopted in NSPFEM (Yuan et al. 2019) is known as ‘‘overly soft’’ or underestimation property and thus offers an upper bound solution (Yuan et al. 2019; Zeng and Liu 2018; Zhang et al. 2018a).

As illustrated in Fig. 1(e), the problem domain Ω is divided into a set of N_n non-overlapping smoothing domains and no gap between each other. The smoothing cell for the particle k is created by sequentially connecting the midpoint of each edge to the centre of the surrounding triangular elements associated with particle k. Therefore, the strain tensor $\tilde{\boldsymbol{\varepsilon}}_k$ for the particle k, i.e., the smoothed strain on the cell Ω^k, can be obtained as

$$\tilde{\boldsymbol{\varepsilon}}_k = \sum_{I \in N^k} \tilde{\mathbf{B}}_I(x^k)\mathbf{u}_I \tag{3}$$

where I is the node number, x is the coordinate, N^k is the number of nodes that are directly connected to particle k, $\mathbf{u}_I$ is the nodal displacements and $\tilde{\mathbf{B}}$ is termed as the smoothed strain–displacement matrix. For 3-node triangular elements, $\tilde{\mathbf{B}}$ can be calculated as,

$$\tilde{\mathbf{B}}_I(x_k) = \frac{1}{A^k}\sum_{j=1}^{N_e^k}\frac{1}{3}A_e^j\mathbf{B}_j \tag{4}$$

where N_e^k is the number of elements related to particle k, j is the element numbering, A_e^j and $\mathbf{B}_j$ are the area and strain gradient matrix of the jth triangular element related to particle k, respectively, and A^k is calculated by

$$A^k = \int_{\Omega^k} d\Omega = \frac{1}{3}\sum_{j=1}^{N_e^k} A_e^j \tag{5}$$

2.4 Equilibrium equation and spatial discretisation for SPFEMs

According to the principle of virtual displacement, the weak form of equilibrium equation is given:

$$\int_V \left(\rho\delta\mathbf{u}^T\mathbf{a} + \left(\mathbf{L}\delta\mathbf{u}\right)^T\boldsymbol{\sigma}\right)dV = \int_S \delta\mathbf{u}^T\mathbf{t}_s dS + \int_V \rho\delta\mathbf{u}^T\mathbf{g}dV \tag{6}$$

in which ρ is the material density, $\boldsymbol{\sigma}$ is stress vector, $\mathbf{u}$ is the test function, **n** is the outward unit vector on the boundary of the body, **a** is the acceleration, and $\mathbf{t}_s$ is the prescribed traction. **L** is operator matrix expressed as

$$\mathbf{L}^T = \begin{bmatrix} \frac{\partial}{\partial x} & 0 & 0 & \frac{\partial}{\partial y} & 0 & \frac{\partial}{\partial z} \\ 0 & \frac{\partial}{\partial y} & 0 & \frac{\partial}{\partial x} & \frac{\partial}{\partial z} & 0 \\ 0 & 0 & \frac{\partial}{\partial z} & 0 & \frac{\partial}{\partial y} & \frac{\partial}{\partial x} \end{bmatrix} \tag{7}$$

To solve Eq.(6), it should be spatially discretised by finite elements. Note that the 3-node triangular element is used instead of six-node triangle element in original PFEM. By introducing the shape function N, the continuous displacement field $\tilde{\mathbf{u}}$ within the element is expressed as:

$$\tilde{\mathbf{u}} = \mathbf{N}\cdot\mathbf{u} \tag{8}$$

Then, the Eq.(6) can be written as:

$$\mathbf{M}\ddot{\mathbf{u}} = \mathbf{F} \tag{9}$$

where $\mathbf{u}$ is the global displacement for all nodes in each degree of freedoms (dofs) and $\ddot{\mathbf{u}}$ is the acceleration; $\mathbf{M}$ is the mass matrix; $\mathbf{F}$ is the global force vector, which is always equal to the difference between the external force $\mathbf{f}_{\text{ext}}$ and internal force $\mathbf{f}_{\text{int}}$.

2.5 Solution algorithm for SPFEMs

The explicit time integration scheme is used for two primary reasons: (1) ease of implementation and (2) ability to avoid massive computation cost when solving large-scale problems.

The central difference time integration scheme used in the SPFEM is summarised in the following box.

Initialise $\dot{\mathbf{u}}^0$ and $\ddot{\mathbf{u}}^0$

Calculate the lumped mass matrix: M

Calculate : $\dot{\mathbf{u}}^{\frac{1}{2}t} = \dot{\mathbf{u}}^0 + \frac{1}{2}\Delta t\ddot{\mathbf{u}}^0$

For each time step:

(1) Update the total displacements: $\mathbf{u}^{t+\Delta t} = \mathbf{u}^t + \Delta t\dot{\mathbf{u}}^{t+\frac{1}{2}\Delta t}$

(2) Calculate the displacement increment: $\Delta\mathbf{u}=\mathbf{u}^{t+\Delta t} - \mathbf{u}^t$

(3) For each integration point *i*:

-Calculate the strain increment: $\Delta\mathbf{u} \rightarrow \Delta\boldsymbol{\varepsilon}_i$

-Calculate the stress increment: $\Delta\boldsymbol{\varepsilon}_i \rightarrow \Delta\boldsymbol{\sigma}_i$

-Update the total stress: $\boldsymbol{\sigma}_i^{t+\Delta t}=\boldsymbol{\sigma}_i^t+\Delta\boldsymbol{\sigma}_i$

(4) Calculate the internal force vector: $\mathbf{f}_{\text{int}}^{t+\Delta t}=\sum_{e=1}^{n_e}\sum_{i=1}^{n_i}\omega_i \det\left(\mathbf{J}_i\right)\mathbf{B}_i^{\mathrm{T}}\boldsymbol{\sigma}_i$

(5) Solve for the new accelerations: $\ddot{\mathbf{u}}^{t+\Delta t}=\mathbf{M}^{-1}\left(\mathbf{f}_{\text{ext}}^{t+\Delta t} - \mathbf{f}_{\text{int}}^{t+\Delta t}\right)$

(6) Update the velocities: $\dot{\mathbf{u}}^{t+\frac{3}{2}\Delta t} = \dot{\mathbf{u}}^{t+\frac{1}{2}\Delta t} + \Delta t\ddot{\mathbf{u}}^{t+\Delta t}$

Explicit time integration scheme is conditionally stable. The time step size should be smaller than a critical value to ensure the stability. The critical value of time step size Δt_{stable} is given by

$$\Delta t_{\text{stable}} = \alpha \frac{l_{\min}}{c} \tag{10}$$

where l_{min} is the characteristic length of the element. For triangular element, the l_{min} is the minimum height for all triangle elements; c is wave propagation speed which can be approximately estimated by $c=\sqrt{(\lambda+2\mu)/\rho}$ (where ρ is material density, λ and μ are Lamé's constants) and α is reduction factor, which is usually equal $1/\sqrt{2}$ ~1.0 according to ABAQUS (Hibbitt et al. 2002), and in this study, α=0.8 was adopted. Since the l_{min} is changing during the simulation process, the adaptive time step scheme in which the critical time step is calculated according to the l_{min} in each step was utilized. To prevent the situation when the time step approaches zero, a minimum stable time step is defined as 0.2 times of initial stable time step. Note that the minimum stable time step is not fixed, which can be adjusted according to the practical problems.

In fact, the validations of both adopted methods (NSPFEM and ESPFEM) have been conducted on simulating four different cases: (1) the vibration of a bar; (2) the soil collapse; (3) the penetration

of a footing in soft soil; and (4) the slope failure by strength reduction. The details of such validations can be found in (Yuan et al. 2019) and (Jin et al. 2020).

2.6 Constitutive model adopted for SPFEMs

To describe the undrained behaviour of sensitive clay, a strain-softening Mohr–Coulomb (MC) model by (Soga et al. 2015) was adopted for both SPFEMs. The model is under the framework of elastoplasticity. The elastic part is general Hook's law requiring two input parameters (Young's modulus E and Poisson's ratio ν), and plastic part follows the non-associated flow rule with three parameters (friction angle ϕ, dilation angle ψ and cohesion c). The MC yield criterion f and plastic potential g are written in principal stresses as follow

$$f = (\sigma_1 - \sigma_3) + (\sigma_1 + \sigma_3)\sin\phi - 2c\cos\psi \tag{11}$$

$$g = (\sigma_1 - \sigma_3) + (\sigma_1 + \sigma_3)\sin\psi \tag{12}$$

Due to the existence of apex point at the yield surface, the integration solution of MC model is always a problem. According to (Clausen et al. 2007), an efficient return algorithm for stress update was adopted for numerically integrating the non-associated MC model. The source code for MC model used in the following cases is available at http://alum.sharif.ir/~koohsari/doc/M-C_by_Johan_Clausen.for. All readers who are interesting on large deformation simulation can reproduce the presented cases by the proposed SPFEM with this MC model.

According to (Soga et al. 2015), the softening behaviour of MC model is achieved by reducing the effective strength parameters (friction angle, ϕ, and cohesion, c) with the accumulated equivalent plastic strain $\varepsilon_{\mathrm{eq}}^{p}$ (PEEQ) according to the following exponential softening rules:

$$\begin{aligned} \phi &= \phi_r + (\phi_p - \phi_r)\, e^{-\eta \varepsilon_{\mathrm{eq}}^{p}} \\ c &= c_r + (c_p - c_r)\, e^{-\eta \varepsilon_{\mathrm{eq}}^{p}} \end{aligned} \tag{13}$$

where the subscripts "r" and "p" represent the residual and peak values, respectively; η is shape factor to control the rate of decrease. The deviatoric plastic strain invariant $\varepsilon_{\mathrm{eq}}^{p}$ is defined as

$$\varepsilon_{\mathrm{eq}}^{p}=\sqrt{\frac{2}{3}\mathbf{e}^{p}:\mathbf{e}^{p}} \tag{14}$$

where **e** is the deviatoric strain tensor.

According to (Yin et al. 2011), the reduction formulation in Eq.(13) is similar to the evolution of soil destructuration for sensitive clays. Coincidentally, the retrogressive failure of landslide usually occurs in such sensitive clays under undrained conditions. Thus, the adopted strength reduction law is particularly suitable to simulate this retrogressive failure.

3 Modelling of retrogressive failure of landslide

To show the performance of both SPFEMs, the retrogressive failure of a landslide of sensitive clay, one of the typical problems in geotechnical engineering involving large deformation, was simulated.

In regions covered by sensitive clays, retrogressive landslides generally occur in gently inclined slopes, as seen in Scandinavia and eastern Canada (Locat et al. 2011). To illustrate the performance of both SPFEMs when modelling such a geohazard, a slope on a sensitive clay deposit is considered, as shown in Fig. 2(a). To simulate the triggering mechanism of progressive failure by erosion or excavation, an eroded block of soil near the slope's toe is first fixed in the gravity stress generation and then the fixed boundary is removed, an approach similar to those seen in (Dey et al. 2015b) and (Yuan et al. 2020).

For soft sensitive clay, the following parameters, based on (Zhang et al. 2017), are adopted for the simulation: Young's modulus E=1×10^3 kPa, friction angle ϕ=0° assuming the undrained shear strength totally taking by the cohesion, dilatancy angle ψ=0° , peak cohesion c_{p}=22 kPa and residual cohesion c_{r}=1.2 kPa, and shape factor η=3 – approximately equivalent to the value of linear reduction relationship adopted by (Zhang et al. 2017) and (Wang et al. 2016). Soil density is ρ =1.7×10^3 kg/m^3. To achieve an approximate undrained condition, the Poisson's ratio υ is set to 0.49, as used by (Tran and Sołowski 2019) in MPM simulation of retrogressive failure of landslide. The frictional coefficient μ between the sensitive clay and the rigid bottom surface is set to 0.3, consistent with the value used by (Wang et al. 2016).

To investigate the influence of mesh density on numerical solutions for two SPFEMs, totals of 5232, 9153 and 13698 particles (9989, 17696 and 27277 three-node triangular elements) are used to discretise the initial problem domain, respectively – equivalent to three different mesh sizes (0.2 m, 0.15 m and 0.12 m), as shown in Fig. 2 (b, c, d). For all simulations, the initial time step is 0.001 s and the simulation proceeds until the final deposit is obtained. The initial stress is generated by gravity loading. A Poisson's ratio of 0.3 is first set to ensure a coefficient of lateral earth pressure at rest, K_0, close to 0.5. Because the undrained condition is necessary for progressive failure (Locat et al. 2013; Locat et al. 2011), after geostress generation the Poisson's ratio υ is changed to 0.49 (Dey et al. 2015b; Quinn et al. 2012; Tran and Sołowski 2019).

4 Results and comparison

4.1 ESPFEM results

To accurately determine the end of retrogressive failure, the horizontal velocity of the sliding front and the maximum velocity are recorded, as depicted in Fig. 3 (a, b). As can be seen, the maximum horizontal velocity is not always at the sliding front, consistent with the findings of (Zhang et al. 2017). The results indicate that the front and maximum horizontal velocities decrease as the mesh density increases. The collapse process and development of retrogressive failures with ESPFEM for different mesh densities are illustrated in Fig. 4, with the coloured contours representing the accumulated equivalent plastic strain (PEEQ). In practice, collapse is triggered by removal of the soil of the toe, commonly by erosion or excavation (Locat et al. 2011). As illustrated, with the first retrogressive collapse C1 moving far from the new slip surface, the second retrogressive collapse C2 occurs, followed by the third retrogressive collapse C3. As Fig. 4 shows, the first slide's location moves further forward as mesh density increases. The type of retrogressive landslide simulated by ESPFEM is more likely soil flow with circle sliding. As the landslide continues, two shear bands originate from the bottom and propagate towards the top surface and the front inclined surface, respectively, producing a graben (see Fig. 4(c-3, c-4)). The type of retrogressive failure simulated by ESPFEM is more likely spread with horsts and grabens (see Fig. 4(c-5)). Because of the friction between collapse and ground, the retrogressive collapse cannot occur indefinitely (as Fig. 3 shows, the maximum horizontal velocity is close to zero at 30 s.). Deposit of

considerable mass in front of the new slope surface stops further retrogressive collapse. The final configuration of the slope, shown in Fig. 4(a-5) and (c-5), indicates that most of the clay involved in the collapses has been remoulded.

For all ESPFEM simulations, the slope collapses progressively four times, with each retrogressive collapse numbered sequentially, using "C+number", and the corresponding occurrence time recorded. An obvious result is that the width of the shear band narrows with increased mesh density. Fig. 5(a) shows the occurrence time of each new retrogressive collapse for three different mesh densities, demonstrating that retrogressive slope failure occurs early on as mesh density increases. Consequently, the landslide will end soon.

The run-out and retrogressive distances are important in assessing the landslide's effects on surrounding buildings. Fig. 6(a) shows both with the final configuration for three different mesh densities as simulated by ESPFEM, indicating that both run-out and retrogressive distances decrease as mesh density increases. The longer retrogressive distance for the coarse mesh in part reflects the wide shear band.

All results demonstrate that the dense mesh, not surprisingly, produces in good simulation performance, at great computational cost. For this case using ESPFEM, simulations with mesh size 0.15 m and 0.12 m are satisfactory but have problems with mesh dependency (see Fig. 6(a)).

4.2 NSPFEM results and comparison with ESPFEM

The same three cases were also simulated by NSPFEM, with the evolution of the sliding front's horizontal and maximum velocities shown in Fig. 3 (c, d). The results are similar to those obtained by ESPFEM simulation, with front and maximum horizontal velocities slightly decreasing as mesh density increases. The velocity evolutions for results with mesh sizes 0.15 m and 0.12 m were almost identical.

The collapse process and development of retrogressive failures for different mesh densities as simulated by NSPFEM are illustrated in Fig. 7. The occurrence position of the first slide moves slightly backwards as mesh density increases, in contrast to the trend seen in ESPFEM simulation. The type of retrogressive failure simulated by NSPFEM for the first slide is spread with horst and graben (see Fig. 7(a-1)), different from that simulated by ESPFEM. For simulation with mesh size

0.2 m, retrogressive collapses occur four times (see Fig. 7(a)), consistent with the results simulated by ESPFEM. However, the number of retrogressive collapses is reduced to three as mesh density increases (see Fig. 7(b) and Fig. 7(c)). The time of occurrence for new retrogressive collapse in three simulations is presented in Fig. 5(b), indicating that the landslides lag as the mesh density increases, contrary to the results of ESPFEM simulation.

Fig. 6(b) shows the run-out and retrogression distances with the final configuration for three different mesh densities as simulated by NSPFEM. The results are again similar: both run-out and retrogression distances decrease with increasing mesh density. Furthermore, the run-out and retrogression distances for simulations with mesh sizes of 0.15 m and 0.12 m are almost identical.

All results again demonstrate that dense mesh produces good simulation performance. NSPFEM simulations with mesh sizes 0.15 m and 0.12 m are satisfactory and have less problem with mesh dependency than ESPFEM.

To further compare the results obtained by ESPFEM and NSPFEM simulation, fine mesh (0.12 m) simulations were selected for both approaches, with Fig. 8 comparing velocity evolution for the two. Both front and maximum velocity were larger under NSPFEM simulation than under ESPFEM, and times for stop of front point and end of retrogressive failure are almost identical for both methods.

The collapse process and development of retrogressive failure, as simulated by ESPFEM and NSPFEM at the same time, are illustrated in Fig. 9. The type of retrogressive landslide seen for the first collapse C1 under ESPFEM simulation is more likely soil flow, and the failure type for the first collapse C1 under NSPFEM is more likely spread with horst and graben. Furthermore, the position of the first retrogressive collapse is farther back for NSPFEM than ESPFEM. For ESPFEM, the strain smoothing domain is one three-node triangular element, whereas the strain smoothing domain for NSPFEM has contributions from several surrounding elements (a third of the area for each element). In general, the smooth domain of NSPFEM is larger than that of ESPFEM for the same mesh, so that more elements are affected during retrogressive collapse under NSPFEM, causing rougher-edged horsts and grabens than under ESPFEM. Furthermore, the number of smoothing domains relating to node number for NSPFEM is less than the number associated with element

number (ESPFEM). According to the weakened weak (W^2) formulation theory, a SPFEM model is softer, generally speaking, when the number of the smoothing domain is less. As a result, the NSPFEM gives an upper bound but the ESPFEM gives an ultra-accurate solution (Liu and Trung 2016; Zeng and Liu 2018). Fig. 10(a) compares the run-out and retrogressive distances at the final configuration for both SPFEMs, which differ little.

Finally, Fig. 10(b) compares CPU time for two calculations, indicating a faster speed for NSPFEM. Unlike ESPFEM, NSPFEM need not transfer variables from old mesh to new and thus saves much calculation time by performing more rapid calculations.

4.3 Influence of shape factor relating to soil destructuration

To investigate the effect of the shape factor, which controls the destructuration rate of soil structure, on retrogressive failure, problems with varying shape factor of η=1, 3 and 5 were simulated by ESPFEM and NSPFEM using only fine mesh, with other material parameters the same as previously described. The collapse process and development of retrogressive failures simulated by ESPFEM and NSPFEM under different shape factors are illustrated in Fig. 11. A comparison of run-out and retrogression distances for different shape factors is shown in Fig. 12. For both SPFEMs, the run-out and retrogression distances increase with the shape factor. A higher shape factor represents a more rapid destructuration rate, resulting in longer run-out and retrogression distances. For a small value of shape factor (η = 1.0), longer run-out and retrogression distances are found with ESPFEM than with NSPFEM. For a large value of shape factor (η = 5.0), ESPFEM gives a longer run-out distance than NSPFEM, but both give an approximately equal retrogression distance.

4.4 Discussion

Compared with the original PFEM adopting a high-order triangular element (e.g., six-node), the main advantage of both SPFEMs is their use of a lower-order triangular element (three-node) while preserving the same level of accuracy – but without suffering volumetric locking. For ESPFEM, frequent variable mapping is still seen in PFEM between the old mesh and the new, representing the predominant computational cost in simulating progressive failure. Moreover, computational cost increases quickly with the number of elements when searching for the location of old Gauss points in the new mesh. NSPFEM avoids variable mapping through use of nodal integration with a strain

smoothing technique. Thus NSPFEM is superior to ESPFEM in computational cost when simulating the progressive failure. However, NSPFEM's performance relative to ESPFEM strongly depends on mesh density, as indicated by the simulated results.

Compared with the discrete element method (DEM), which is usually adopted for analysis of large deformation problems, both SPFEMs incur significantly less computational cost for engineering scale problems. Indeed, DEM is rarely used to solve real engineering problems because of the unacceptably large number of soil particles involved, although it has traditionally been used to investigate failure mechanism at small scales (Jiang et al. 2013; Zhang et al. 2019; Zhu et al. 2020).

Compared with other similar numerical methods (e.g., smoothed-particle hydrodynamics [SPH] and MPM), both SPFEMs offer some advantages of accuracy and computational cost. Because both take PFEM as their base, they surpass SPH (Huang and Dai 2014) and MPM (Conte et al. 2019) in accuracy from small strain to large. Furthermore, the problem of boundary conditions encountered in SPH and MPM can be naturally solved using SPFEMs. NSPFEM's computational cost is approximately equivalent to SPH's and MPM's owing to the similar need to search the surrounding particles or elements, but when solving volumetric locking problems using MPM, a strain average approach is usually employed, increasing computational cost. Although remeshing of technology is required for both SPFEMs, calculation time does not significantly increase with some advanced remeshing approaches (Areias et al. 2016; Areias and Rabczuk 2017; Areias et al. 2013; Areias et al. 2018). Variable mapping is needed for MPM and ESPFEM, with MPM's computational cost less than ESPFEM's because the grid search used in MPM is quicker than the global search used in ESPFEM. However, ESPFEM's use of Gauss integration when calculating internal force makes it more accurate than MPM (Jin et al. 2020).

Overall, both SPFEMs have advantages of accuracy and computational cost in simulating progressive failure.

5 Application to simulation of a real progressive failure

In 1994, a sensitive clay landslide occurred in Sainte-Monique, Quebec (Locat et al. 2013; Locat et al. 2015). Fig. 13(a) presents a cross-section of this landslide. The height of the slope is about 17 m, and the inclination is about 24°. The retrogression distance is about 100 m from the

initial crest to the back scarp. The landslide is characterised as spread failure with horsts and grabens observed in the site, according to the landslide classification of (Cruden and Varnes 1996). Direct field measurements showed a horst angle of failure surface of about 60° to the horizontal, corresponding to $45°+\phi/2$ with the horizontal (Locat et al. 2011). More details about the landslide can be found in (Locat et al. 2011), including its morphology and geotechnical properties, the hydraulic conditions of the deposit, and the results of some laboratory tests. Based on investigations by (Liu et al. 2007; Locat et al. 2013; Locat et al. 2015), the undrained shear strength of clay varies from 25 to 40 kPa between the ground surface down to the toe of the slope, so an average value of 35 kPa is used in the simulation; the shear strength of remoulded clay is 0.7 kPa on average; the shape factor η is set to 1.0; the unit weight of the clay equals 16 kN/m^3; the Poisson's ratio υ is set to 0.49 for describing an undrained condition; and Young's modulus is E=1×10^3 kPa for the sensitive clay.

Because NSPFEM's performance is mesh-dependent, a satisfactory result requires numerous particles to discretise the large problem domain. Although NSPFEM performs rapid calculations, dealing with such a large number of particles is difficult. Accordingly, ESPFEM, with its reduced susceptibility to the mesh dependency problem, is selected to simulate the Sainte-Monique spread. The whole problem domain is discretised by 14109 particles with 27166 elements. The bottom boundary is fixed in both directions. The left and right boundaries are fixed in the horizontal direction. The triggering mechanism by erosion is simulated by removing the eroded block. The initial stress condition is generated by gravity loading with an earth pressure coefficient K_0 = 0.5 (Tran and Sołowski 2019). The initial time step is 0.0005 s. The calculation time for whole progressive failure by ESPFEM is about 6.82 hours on an Intel Core i9-9900K running at 3.60 GHz, with 64.0 GB of RAM.

Because MPM also has the ability to analyse real-world problems such as this one (Conte et al. 2020; Li et al. 2016), this case was also previously simulated using MPM (Tran and Sołowski 2019). Approximately 500,000 material points are needed to obtain accurate results, extending calculation time beyond that seen with ESPFEM.

Fig. 13(b) compares the ground levels observed on site and in the numerical model, showing that the basic ground level profile after the progressive landslide is well captured by ESPFEM. Both

the retrogression and run-out distances are accurately predicted. Fig. 14 shows evolutions in maximum velocity and kinematic energy with time for the Sainte-Monique progressive landslide. Three main collapses during the whole landslide can be clearly seen, with the final configuration obtained at about 42 s. Fig. 15 presents numerical results from the initial condition to several post-failure states of the landslide at 6.34 s, 10.32 s, 14.51 s, 24.09 s and 42.8 s with the PEEQ contour. ESPFEM accurately portrays the formation and propagation of the horizontal and inclined shear bands and well reproduces the horsts and grabens that represent the spread failure mode, but the tip of the horsts in the simulation is close to 90°, versus about 60° in the field. This difference between simulations and measurements may be attributed to the adoption of a simple constitutive model unable to comprehensively reflect the characteristics of the sensitive clays. A similar result was obtained by MPM modelling (Tran and Sołowski 2019). All results do demonstrate, however, that ESPFEM can well simulate progressive failure.

6 Conclusions

In this study, a series of numerical analyses was been carried out to investigate the development of retrogressive failures within a landslide. Two typical SPFEMs (an edge-based strain smoothing PFEM, ESPFEM, and a node-based strain smoothing PFEM, NSPFEM) were briefly introduced and then adopted as the numerical tools for their outstanding performance in large deformation analysis.

Retrogressive failure of landslide was modelled using a strain–softening MC model, assuming a Poisson's ratio of 0.49 to describe an undrained condition. The influence of mesh density on development of retrogressive failure was evaluated for two SPFEMs, and numerical analysis of three mesh sizes (0.2 m, 0.15 m and 0.12 m) was carried out sequentially, with all numerical results indicating the following:

(a) The type of retrogressive failure seen in landslide is more likely spread with horsts and grabens for ESPFEM and NSPFEM.

(b) Run-out and retrogression distances decrease as mesh density increases for both methods. For dense mesh, the obtained run-out and retrogression distances for ESPFEM and SPFEM are almost identical.

(c) The number of retrogressive collapses is not affected by mesh density for ESPFEM, whereas it reduces for NSPFEM when increasing mesh density. The shear band of the coarse mesh is wider in both.

(d) Retrogressive collapse occurs earlier with ESPFEM but is delayed in NSPFEM with increases in mesh density.

(e) NSPFEM offers more rapid calculations than ESPFEM and mitigates the mesh dependency problem.

(f) Increases in shape factor relating to soil destructuration can accelerate retrogressive failure in a landslide, increasing run-out and retrogression distances.

Finally, a landslide of sensitive clay in Sainte-Monique, Quebec, was simulated using ESPFEM. The complete upward progressive failure, including the formation and propagation of horsts and grabens, was reproduced. The computational efficiency of ESPFEM was highlighted by comparison with MPM, with ESPFEM's accuracy confirmed by comparing the simulated ground surface to the site ground surface.

Acknowledgements

This research was financially supported by the Research Grants Council (RGC) of Hong Kong Special Administrative Region Government (HKSARG) of China (Grant No.: 15209119, PolyU R5037-18F) and Key Special Project for Introduced Talents Team of Southern Marine Science and Engineering Guangdong Laboratory (Guangzhou) (Grant No.: GML2019ZD0503).

Reference

Areias, P., Msekh, M. & Rabczuk, T. 2016. Damage and fracture algorithm using the screened Poisson equation and local remeshing. Engineering Fracture Mechanics, **158**, 116-143.

Areias, P. & Rabczuk, T. 2017. Steiner-point free edge cutting of tetrahedral meshes with applications in fracture. Finite Elements in Analysis and Design, **132**, 27-41.

Areias, P., Rabczuk, T. & Dias-da-Costa, D. 2013. Element-wise fracture algorithm based on rotation of edges. Engineering Fracture Mechanics, **110**, 113-137.

Areias, P., Reinoso, J., Camanho, P., de Sá, J.C. & Rabczuk, T. 2018. Effective 2D and 3D crack propagation with local mesh refinement and the screened Poisson equation. Engineering Fracture Mechanics, **189**, 339-360.

Carbonell, J.M., Oñate, E. & Suárez, B. 2009. Modeling of ground excavation with the particle finite-element method. Journal of engineering mechanics, **136**, 455-463.

Clausen, J., Damkilde, L. & Andersen, L. 2007. An efficient return algorithm for non-associated plasticity with linear yield criteria in principal stress space. Computers & Structures, **85**, 1795-1807.

Conte, E., Pugliese, L. & Troncone, A. 2019. Post-failure stage simulation of a landslide using the material point method. Engineering Geology, **253**, 149-159, doi: https://doi.org/10.1016/j.enggeo.2019.03.006.

Conte, E., Pugliese, L. & Troncone, A. 2020. Post-failure analysis of the Maierato landslide using the material point method. Engineering Geology, 105788.

Crawford, C.B. 1968. Quick clays of eastern Canada. Engineering Geology, **2**, 239-265, doi: https://doi.org/10.1016/0013-7952(68)90002-1.

Cruden, D. & Varnes, D. 1996. Landslide types and processes: in "Landslides Investigation and Mitigation". Eds K. Turner, RL Schuster. Transportation Research Board Special Report, **247**.

Dey, R., Hawlader, B., Phillips, R. & Soga, K. 2015a. Large deformation finite-element modeling of progressive failure leading to spread in sensitive clay slopes. Géotechnique, **65**, 657-668.

Dey, R., Hawlader, B., Phillips, R. & Soga, K. 2015b. Large deformation finite-element modelling of progressive failure leading to spread in sensitive clay slopes. Géotechnique, **65**, 657-668.

Geertsema, M., Cruden, D.M. & Schwab, J.W. 2006. A large rapid landslide in sensitive glaciomarine sediments at Mink Creek, northwestern British Columbia, Canada. Engineering Geology, **83**, 36-63, doi: https://doi.org/10.1016/j.enggeo.2005.06.036.

Hibbitt, K., Karlsson, B. & Sorensen, P. 2002. ABAQUS/Explicit user's manual (version 10.0). Hibbitt, Karlsson & Sorensen, Inc., Pawtucket, RI.

Huang, Y. & Dai, Z. 2014. Large deformation and failure simulations for geo-disasters using smoothed particle hydrodynamics method. Engineering Geology, **168**, 86-97, doi: https://doi.org/10.1016/j.enggeo.2013.10.022.

Jiang, M.J., Liu, J.D., Sun, Y.G. & Yin, Z.Y. 2013. Investigation into macroscopic and microscopic behaviors of bonded sands using distinct element method. Soils and Foundations, **53**, 804-819, doi: 10.1016/j.sandf.2013.10.001.

Jin, Y.-F., Wu, Z.-X., Yin, Z.-Y. & Shen, J.S. 2017. Estimation of critical state-related formula in advanced constitutive modeling of granular material. Acta Geotechnica, **12**, 1329-1351, doi: 10.1007/s11440-017-0586-5.

Jin, Y.-F., Yin, Z.-Y., Wu, Z.-X. & Daouadji, A. 2018a. Numerical modeling of pile penetration in silica sands considering the effect of grain breakage. Finite Elements in Analysis and Design, **144**, 15-29, doi: https://doi.org/10.1016/j.finel.2018.02.003.

Jin, Y.-F., Yin, Z.-Y., Wu, Z.-X. & Zhou, W.-H. 2018b. Identifying parameters of easily crushable sand and application to offshore pile driving. Ocean Engineering, **154**, 416-429, doi: 10.1016/j.oceaneng.2018.01.023.

Jin, Y.-F., Yin, Z.-Y., Zhou, W.-H. & Huang, H.-W. 2019. Multi-objective optimization-based updating of predictions during excavation. Engineering Applications of Artificial Intelligence, **78**, 102-123, doi: https://doi.org/10.1016/j.engappai.2018.11.002.

Jin, Y.-F., Yuan, W.-H., Yin, Z.-Y. & Cheng, Y.-M. 2020. An edge-based strain smoothing particle finite element method for large deformation problems in geotechnical engineering. International Journal for Numerical and Analytical Methods in Geomechanics, **44**, 923-941, doi: 10.1002/nag.3016.

Karlsrud, K., Aas, G. & Gregersen, O. 1985. Can we predict landslide hazards in soft sensitive clays? Summary of Norwegian practice and experiences. Publikasjon-Norges Geotekniske Institutt.

Lee, C. & Lee, P.-S. 2018. A new strain smoothing method for triangular and tetrahedral finite elements. Computer Methods in Applied Mechanics and Engineering, **341**, 939-955.

Li, X., Wu, Y., He, S. & Su, L. 2016. Application of the material point method to simulate the post-failure runout processes of the Wangjiayan landslide. Engineering Geology, **212**, 1-9.

Liu, G.-R. & Trung, N.T. 2016. Smoothed finite element methods. CRC press.

Liu, G., Dai, K. & Nguyen, T.T. 2007. A smoothed finite element method for mechanics problems. Computational Mechanics, **39**, 859-877.

Locat, A., Jostad, H.P. & Leroueil, S. 2013. Numerical modeling of progressive failure and its implications for spreads in sensitive clays. Canadian Geotechnical Journal, **50**, 961-978.

Locat, A., Leroueil, S., Bernander, S., Demers, D., Jostad, H.P. & Ouehb, L. 2011. Progressive failures in eastern Canadian and Scandinavian sensitive clays. Canadian Geotechnical Journal, **48**, 1696-1712.

Locat, A., Leroueil, S., Fortin, A., Demers, D. & Jostad, H.P. 2015. The 1994 landslide at Sainte-Monique, Quebec: geotechnical investigation and application of progressive failure analysis. Canadian Geotechnical Journal, **52**, 490-504.

Mohammadi, S. & Taiebat, H. 2016. Finite element simulation of an excavation-triggered landslide using large deformation theory. Engineering Geology, **205**, 62-72, doi: https://doi.org/10.1016/j.enggeo.2016.02.012.

Quinn, P., Diederichs, M., Rowe, R. & Hutchinson, D. 2012. Development of progressive failure in sensitive clay slopes. Canadian Geotechnical Journal, **49**, 782-795.

Shen, S., Wang, Z. & Cheng, W. 2017. Estimation of lateral displacement induced by jet grouting in clayey soils. Géotechnique, **67**, 621-630.

Shen, S.L. & Xu, Y.S. 2011. Numerical evaluation of land subsidence induced by groundwater pumping in Shanghai. Canadian Geotechnical Journal, **48**, 1378-1392.

Soga, K., Alonso, E., Yerro, A., Kumar, K. & Bandara, S. 2015. Trends in large-deformation analysis of landslide mass movements with particular emphasis on the material point method. Géotechnique, **66**, 248-273.

Tavenas, F. 1984. Landslides in Canadian sensitive clays-a state-of-the-art. *Proceedings of the 4th International Symposium on Landslides, Toronto, Ont*, 16-21.

Tran, Q.-A. & Sołowski, W. 2019. Generalized Interpolation Material Point Method modelling of large deformation problems including strain-rate effects–Application to penetration and progressive failure problems. Computers and Geotechnics, **106**, 249-265.

Troncone, A. 2005. Numerical analysis of a landslide in soils with strain-softening behaviour. Géotechnique, **55**, 585-596.

Troncone, A., Conte, E. & Donato, A. 2014. Two and three-dimensional numerical analysis of the progressive failure that occurred in an excavation-induced landslide. Engineering Geology, **183**, 265-275, doi: https://doi.org/10.1016/j.enggeo.2014.08.027.

Wang, B. 2019. Failure mechanism of an ancient sensitive clay landslide in eastern Canada. Landslides, 1-13.

Wang, B., Vardon, P. & Hicks, M. 2016. Investigation of retrogressive and progressive slope failure mechanisms using the material point method. Computers and Geotechnics, **78**, 88-98.

Wang, B., Vardon, P. & Hicks, M. 2018. Rainfall-induced slope collapse with coupled material point method. Engineering Geology, **239**, 1-12.

Wu, Z.-X., Yin, Z.-Y., Jin, Y.-F. & Geng, X.-Y. 2017. A straightforward procedure of parameters determination for sand: a bridge from critical state based constitutive modelling to finite element analysis. European Journal of Environmental and Civil Engineering, 1-23, doi: 10.1080/19648189.2017.1353442.

Yang, J., Yin, Z.-Y., Laouafa, F. & Hicher, P.-Y. 2019a. Analysis of suffusion in cohesionless soils with randomly distributed porosity and fines content. Computers and Geotechnics, **111**, 157-171.

Yang, J., Yin, Z.-Y., Laouafa, F. & Hicher, P.-Y. 2019b. Hydro-mechanical modeling of granular soils considering internal erosion. Canadian Geotechnical Journal.

Yang, J., Yin, Z.-Y., Laouafa, F. & Hicher, P.-Y. 2019c. Modeling coupled erosion and filtration of fine particles in granular media. Acta Geotechnica, 1-13.

Yang, J., Yin, Z.Y., Laouafa, F. & Hicher, P.Y. 2019d. Internal erosion in dike ‐ on ‐ foundation modeled by a coupled hydromechanical approach. International Journal for Numerical and Analytical Methods in Geomechanics, **43**, 663-683.

Yin, Z.-Y., Jin, Y.-F., Shen, J.S. & Hicher, P.-Y. 2018. Optimization techniques for identifying soil parameters in geotechnical engineering: Comparative study and enhancement. International Journal for Numerical and Analytical Methods in Geomechanics, **42**, 70-94, doi: 10.1002/nag.2714.

Yin, Z.Y., Karstunen, M., Chang, C.S., Koskinen, M. & Lojander, M. 2011. Modeling Time-Dependent Behavior of Soft Sensitive Clay. Journal of Geotechnical and Geoenvironmental Engineering, **137**, 1103-1113, doi: 10.1061/(asce)gt.1943-5606.0000527.

Yuan, W.-H., Liu, K., Zhang, W., Dai, B. & Wang, Y. 2020. Dynamic modeling of large deformation slope failure using smoothed particle finite element method. Landslides, 1-13.

Yuan, W.-H., Wang, B., Zhang, W., Jiang, Q. & Feng, X.-T. 2019. Development of an explicit smoothed particle finite element method for geotechnical applications. Computers and Geotechnics, **106**, 42-51.

Zeng, W. & Liu, G. 2018. Smoothed finite element methods (S-FEM): an overview and recent developments. Archives of Computational Methods in Engineering, **25**, 397-435.

Zhang, D.M., Gao, C.P. & Yin, Z.Y. 2019. CFD-DEM modeling of seepage erosion around shield tunnels. Tunnelling and Underground Space Technology, **83**, 60-72, doi: 10.1016/j.tust.2018.09.017.

Zhang, W., Yuan, W. & Dai, B. 2018a. Smoothed Particle Finite-Element Method for Large-Deformation Problems in Geomechanics. International Journal of Geomechanics, **18**, 04018010.

Zhang, X., Krabbenhoft, K. & Sheng, D. 2014. Particle finite element analysis of the granular column collapse problem. Granular Matter, **16**, 609-619.

Zhang, X., Krabbenhoft, K., Sheng, D. & Li, W. 2015. Numerical simulation of a flow-like landslide using the particle finite element method. Computational Mechanics, **55**, 167-177.

Zhang, X., Oñate, E., Torres, S.A.G., Bleyer, J. & Krabbenhoft, K. 2018b. A unified Lagrangian formulation for solid and fluid dynamics and its possibility for modelling submarine landslides and their consequences. Computer Methods in Applied Mechanics and Engineering.

Zhang, X., Sheng, D., Sloan, S.W. & Bleyer, J. 2017. Lagrangian modelling of large deformation induced by progressive failure of sensitive clays with elastoviscoplasticity. International Journal for Numerical Methods in Engineering, **112**, 963-989.

Zhang, X., Sloan, S.W. & Oñate, E. 2018c. Dynamic modelling of retrogressive landslides with emphasis on the role of clay sensitivity. International Journal for Numerical and Analytical Methods in Geomechanics, **42**, 1806-1822.

Zhu, H.X., Yin, Z.Y. & Zhang, Q. 2020. A novel coupled FDM-DEM modelling method for flexible membrane boundary in laboratory tests. International Journal for Numerical and Analytical Methods in Geomechanics, doi: 10.1002/nag.3019.

Zhuang, X., Zhou, S., Sheng, M. & Li, G. 2020. On the hydraulic fracturing in naturally-layered porous media using the phase field method. Engineering Geology, **266**, 105306, doi: https://doi.org/10.1016/j.enggeo.2019.105306.

Figure captions

Fig. 1 Strain-smoothed element method for the 3-node triangular element (after Lee and Lee 2018): (a) strains of a target element and its neighbouring elements; (b) strain smoothing between the target and each neighbouring element; (c) three Gauss integration points in the natural coordinate system (r , s); (d) construction of the smoothed strain field through Gauss points; (e) 3-noded elements and the smoothing domains associated with nodes

Fig. 2 (a) Schematic diagram for the retrogressive failure of a slope and three models with different mesh sizes of for retrogressive failure of landslide: (b) 0.2 m; (c) 0.15 m; (d) 0.12 m

Fig. 3 ~~Evolution of front and maximum velocities in the landslide by ESPFEM~~ Evolution of the landslide front horizontal velocity and maximum velocity: (a, b) ESPFEM; (c, d) NSPFEM

Fig. 4 ~~Retrogressive failure procedures of the slope~~ Evolution of slope retrogressive failure at different calculation times by ESPFEM: (a) mesh size=0.2 m; (b) mesh size=0.15 m; (c) mesh size=0.12 m

Fig. 5 Time at the occurrence of different retrogressive collapses by: (a) ESPFEM; (b) NSPFEM

Fig. 6 Run-out and retrogressive distances at different mesh sizes by: (a) ESPFEM; (b) NSPFEM

Fig. 7 ~~Retrogressive failure procedures of the slope~~ Evolution of slope retrogressive failure at different calculation times by NSPFEM: (a) mesh size=0.2 m; (b) mesh size=0.15 m; (c) mesh size=0.12 m

Fig. 8 Comparison of the evolution of velocities in landslide by two SPFEMs

Fig. 9 Retrogressive failure procedures of the slope at different calculation times by two SPFEMs

Fig. 10 (a) Comparison of run-out and retrogressive distances at the final configuration for two SPFEMs; (b) Comparison of CPU time for two calculations by two SPFEMs

Fig. 11 Final deposits of simulation by two SPFEMs using different shape factors for sensitive clays

Fig. 12 Curves of (a) run-out distance and (b) retrogression distance against shape factor

Fig. 13 (a) Numerical model of the Sainte-Monique spread by SPFEM; (b) Comparison of ground level for the Sainte-Monique spread between measurement and simulation

Fig. 14 Evolution of maximum velocity and kinematic energy of Sainte-Monique spread by SPFEM

Fig. 15 Retrogressive failure of Sainte-Monique spread at different time simulated by ESPFEM

608

609

610 **Figure 1**

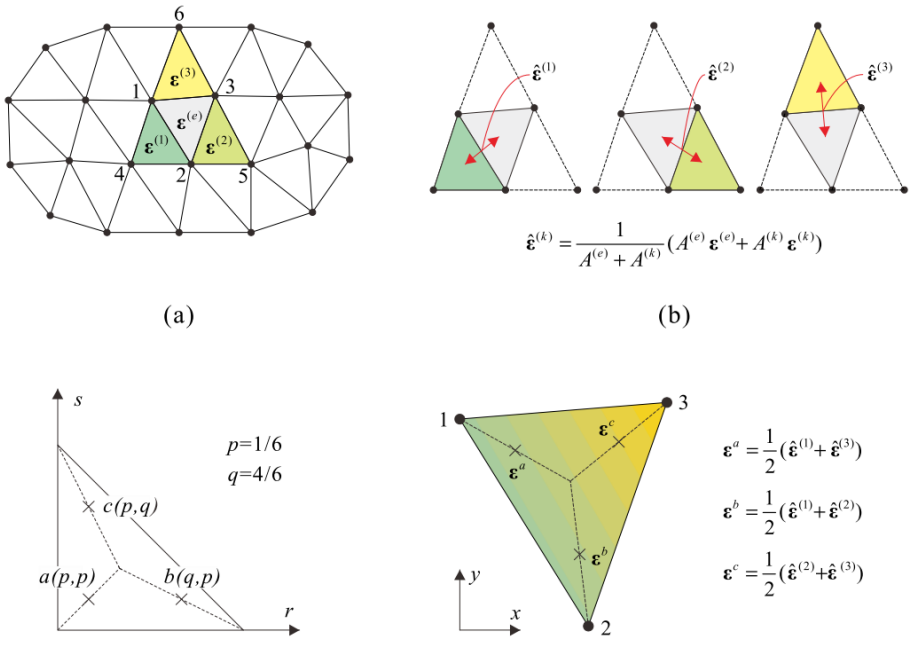

611

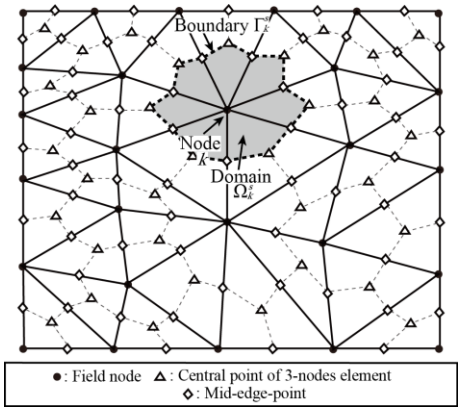

(e)

612

613

614 **Figure 2**

615

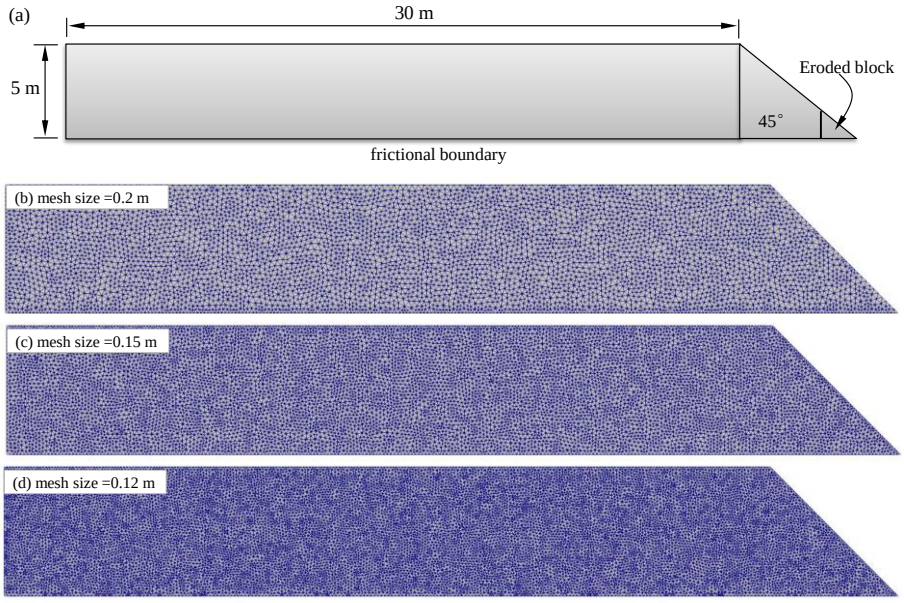

616

617

618 **Figure 3**

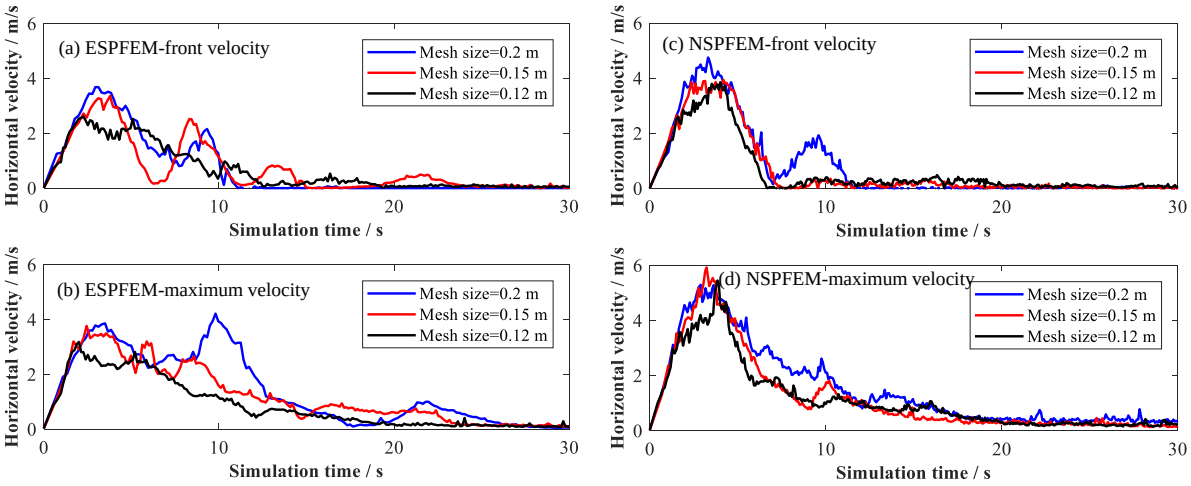

619

620

Figure 4

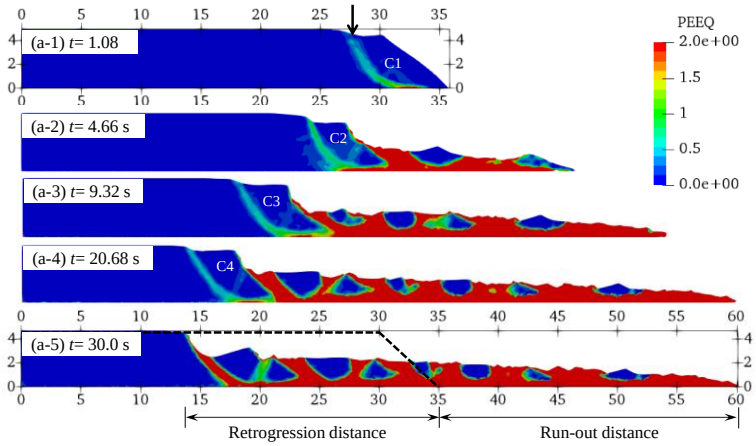

(a) Mesh size =0.2 m

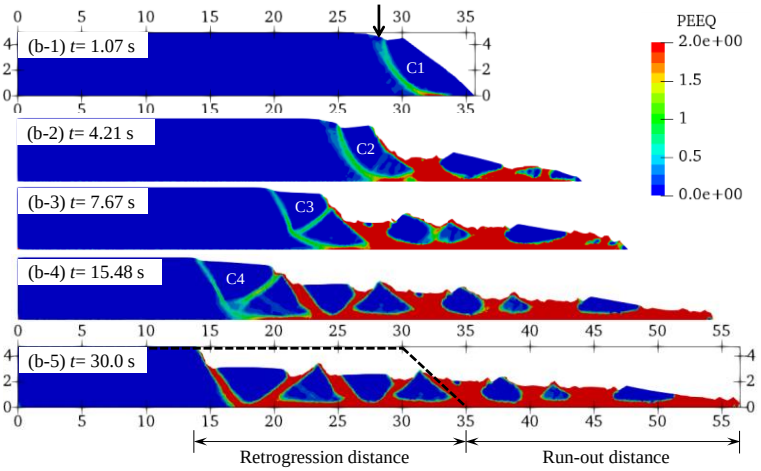

(b) Mesh size=0.15 m

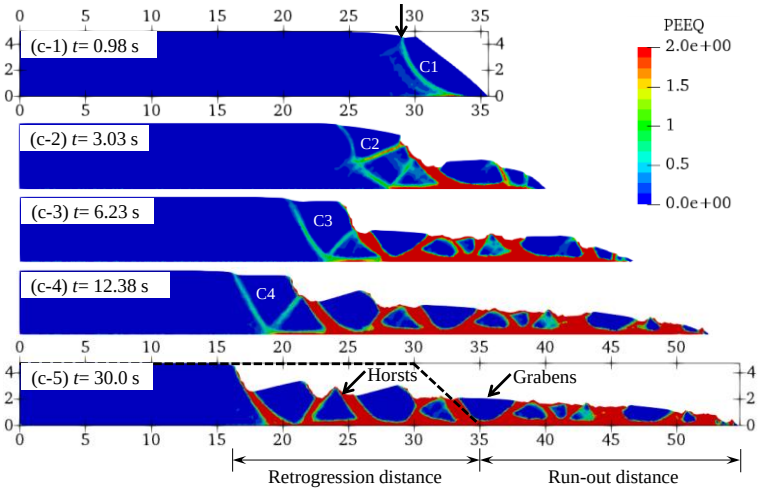

(c) Mesh size =0.12 m

629 **Figure 5**

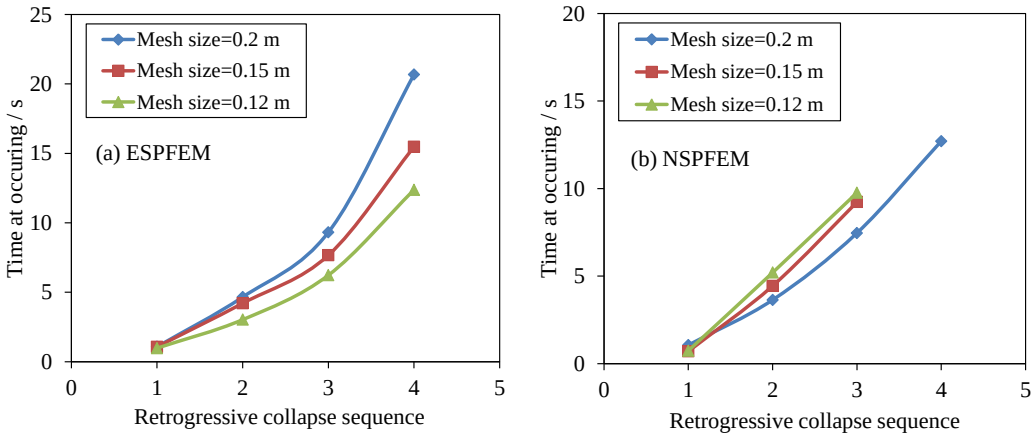

630

631

632

633

634 **Figure 6**

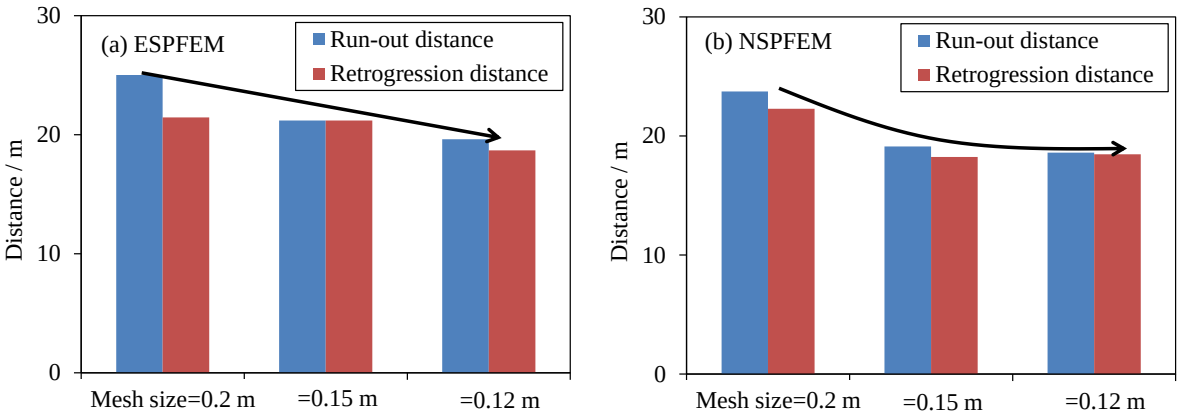

635
636
637
638

Figure 7

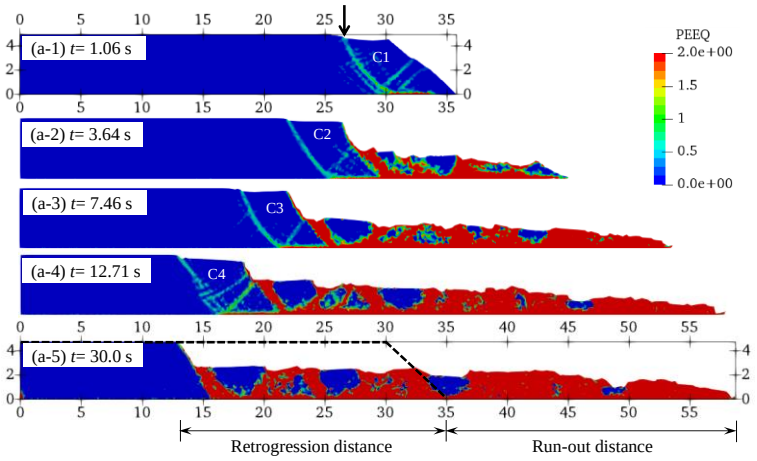

(a) Mesh size =0.2 m

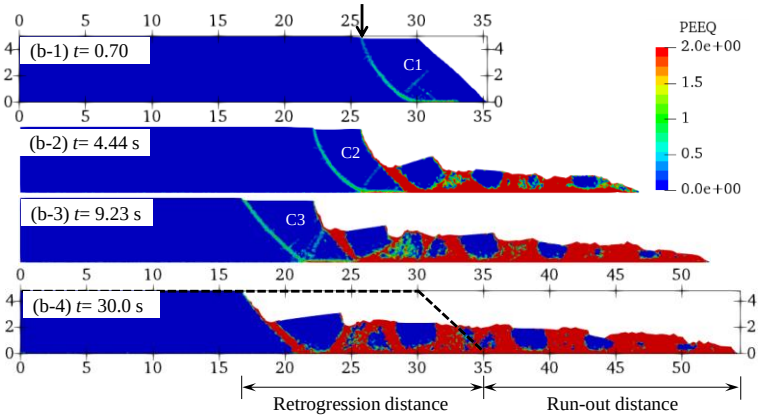

(b) Mesh size =0.15 m

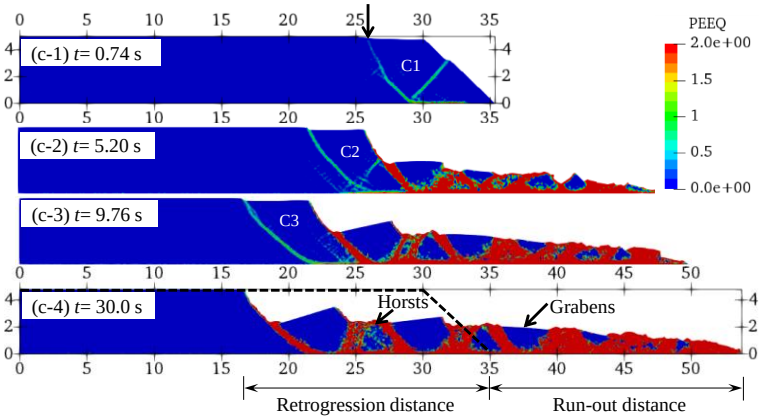

(c) Mesh size=0.12 m

647 **Figure 8**

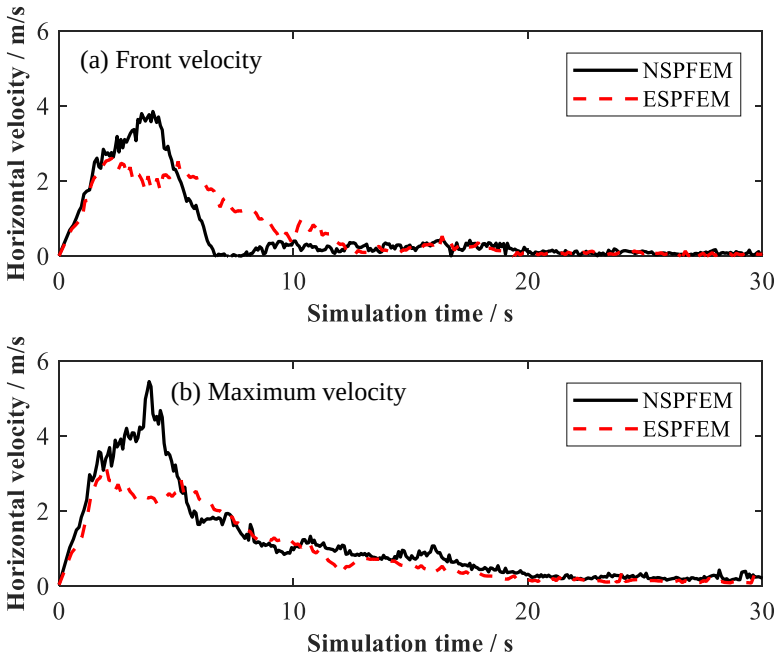

648

649

Figure 9

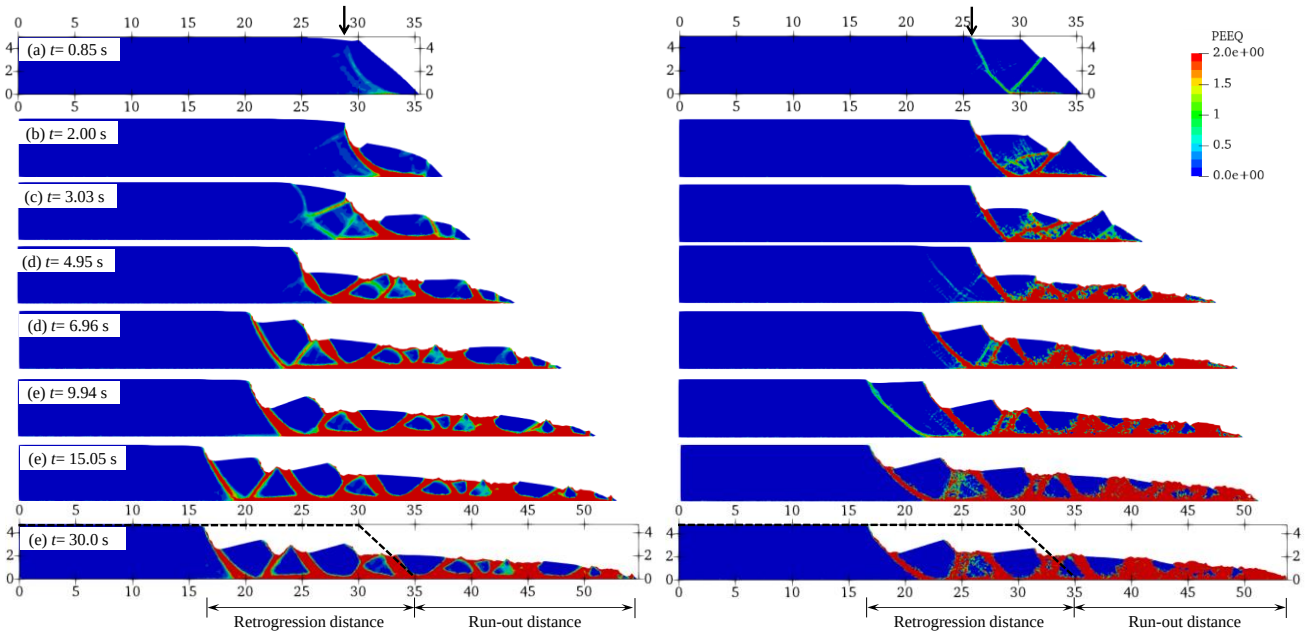

ESPFEM **NSPFEM**

653 **Figure 10**

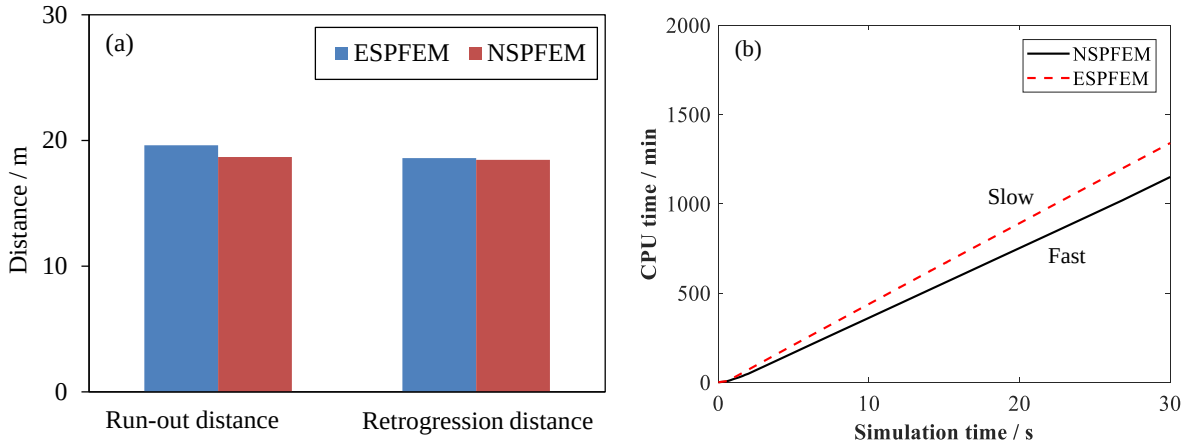

654

655

Figure 11

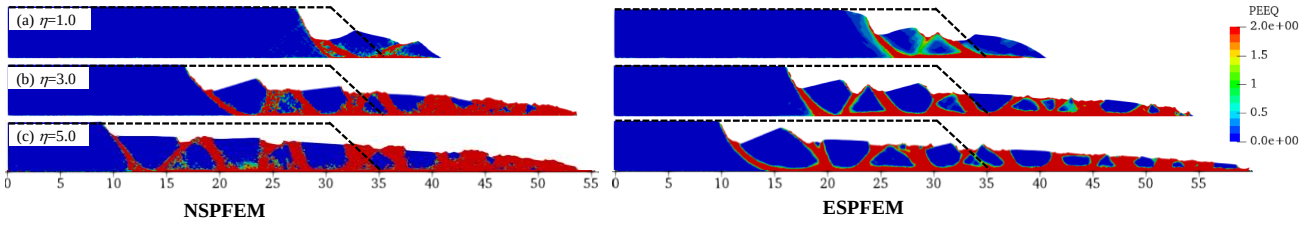

NSPFEM **ESPFEM**

660 **Figure 12**

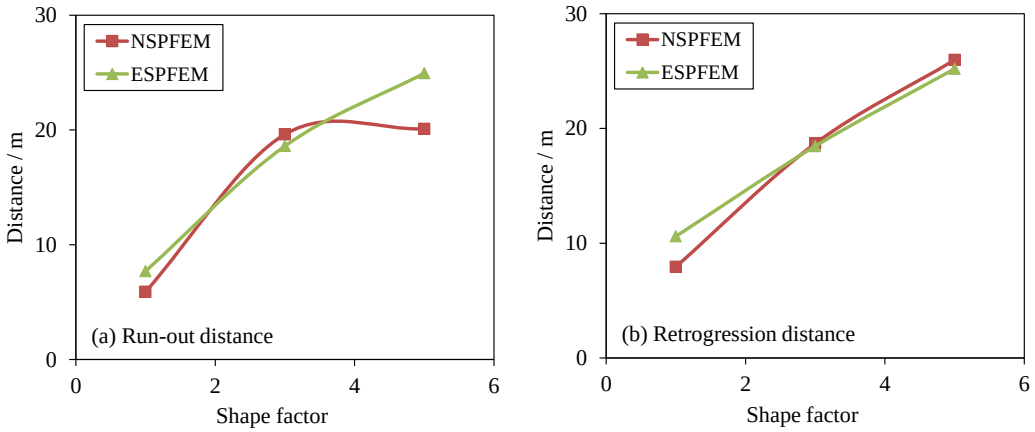

661

662

663

664 **Figure 13**

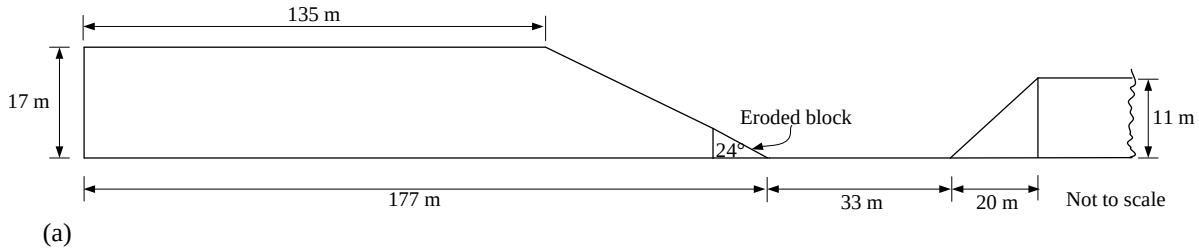

(a)

665

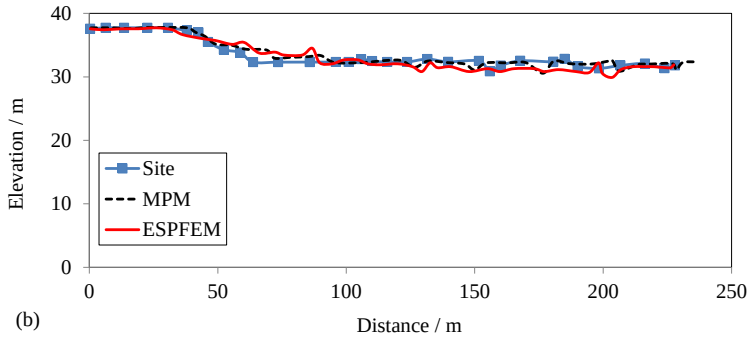

(b)

666

667

668 **Figure 14**

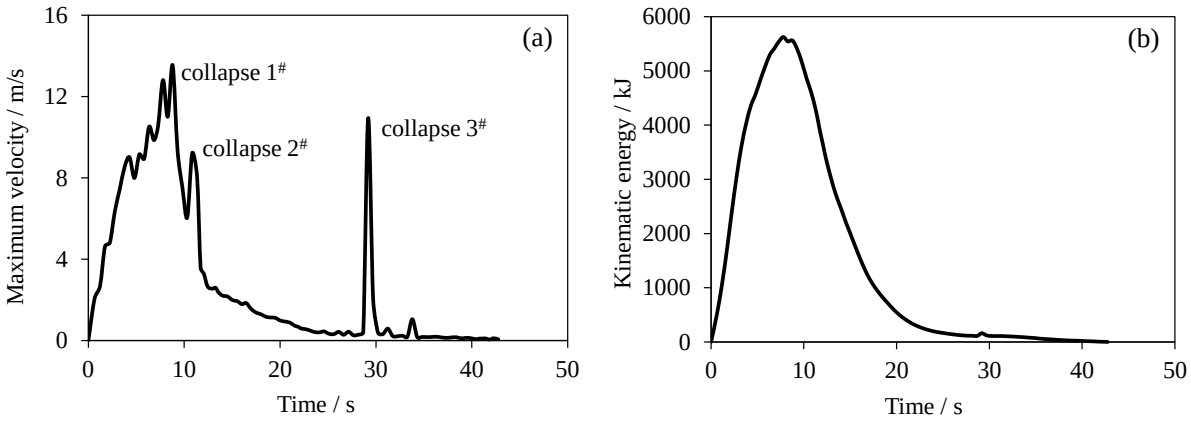

669

670

671 **Figure 15**

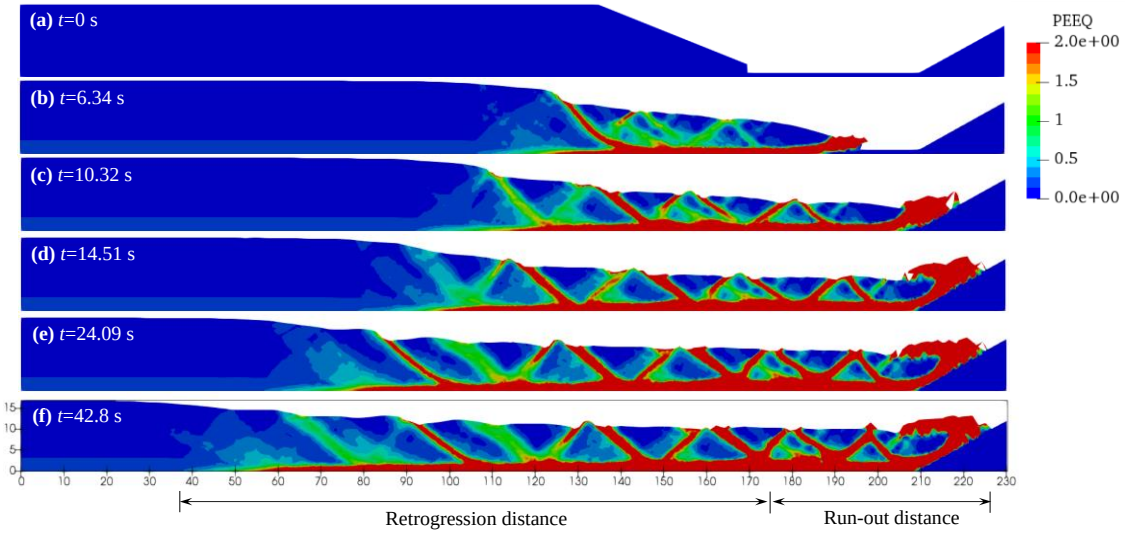

672

673

674